A Cloud-Controlling Factor Perspective on the Hemispheric Asymmetry of Extratropical Cloud Albedo

Joaquín E. Blanco,[a] Rodrigo Caballero,[a] George Datseris,[b] Bjorn Stevens,[b] Sandrine Bony,[c] Or Hadas,[d] and Yohai Kaspi[d]

[a] *Department of Meteorology and Bolin Centre for Climate Research, Stockholm University, Stockholm, Sweden*
[b] *Max Planck Institute for Meteorology, Hamburg, Germany*
[c] *LMD/IPSL, CNRS, Sorbonne University, Paris, France*
[d] *Department of Earth and Planetary Sciences, Weizmann Institute of Science, Rehovot, Israel*

ABSTRACT: The Northern and Southern Hemispheres reflect on average almost equal amounts of sunlight due to compensating hemispheric asymmetries in clear-sky and cloud albedo. Recent work indicates that the cloud albedo asymmetry is largely due to clouds in extratropical oceanic regions. Here, we investigate the proximate causes of this extratropical cloud albedo asymmetry using a cloud-controlling factor (CCF) approach. We develop a simple index that measures the skill of CCFs, either individually or in combination, in predicting the asymmetry. The index captures the contribution to the asymmetry due to interhemispheric differences in the probability distribution function of daily CCF values. Cloud albedo is quantified using daily MODIS satellite retrievals, and is related to range of CCFs derived from the ERA5 product. We find that sea surface temperature is the CCF that individually explains the largest fraction of the asymmetry, followed by surface wind. The asymmetry is predominantly due to low clouds, and our results are consistent with prior local-scale modeling work showing that marine boundary layer clouds become thicker and more extensive as surface wind increases and surface temperature cools. The asymmetry is consistent with large-scale control of storm-track intensity and surface winds by meridional temperature gradients: persistently cold and windy conditions in the Southern Hemisphere keep cloud albedo high year-round. Our results have important implications for global-scale cloud feedbacks and contribute to efforts to develop a theory for planetary albedo and its symmetry.

KEYWORDS: Extratropics; Southern Ocean; Clouds; Wind; Albedo; Satellite observations

1. Introduction

Clouds are fundamental to most aspects of climate. They are a key component of Earth's hydrologic cycle and have a profound effect on the global radiation budget. Clouds have long been studied in terms of geographical and seasonal variations as well as their connections to dynamics and thermodynamics (Riehl 1947; Young 1967; Norris 1998a,b; Houze 2014). The Southern Ocean is one of the cloudiest places of our planet, with a cloud cover fraction of about 0.8 year-round (Haynes et al. 2011; IPCC 2013; McCoy et al. 2014). A number of recent studies have examined various aspects of Southern Ocean clouds: large-scale controls on cloudiness, the relation between cloud albedo and cloud fraction, structure and microphysical properties, and cloud biases in climate models (Bodas-Salcedo et al. 2012, 2014, 2016; Haynes et al. 2011; McCoy et al. 2014; Bender et al. 2017; Wall et al. 2017a,b).

Here, we address the question of how and why Southern Ocean cloud albedo differs from that in Northern Hemisphere oceans at similar latitudes. Interest in this question is motivated by the fact, known since the early days of satellite

Earth observation, that the Northern and Southern Hemispheres reflect the same amount of sunlight to within observational error (Vonder Haar and Suomi 1971). This hemispheric symmetry in reflected insolation has been confirmed by subsequent generations of satellites; the most recent observations estimate the interhemispheric difference in hemispherically averaged reflected shortwave radiation at around 0.2 W m^{-2} in the annual mean, equivalent to ~0.2% of the global mean (Stevens and Schwartz 2012; Voigt et al. 2013; Stephens et al. 2015). Since annual-mean insolation is exactly symmetric around the equator, these observations imply that Earth's planetary albedo is also almost perfectly symmetric, at least in the hemispheric mean.

This symmetry is surprising given the obvious surface asymmetry between the two hemispheres: land and sea ice cover roughly 40% of the Northern Hemisphere (NH) but only 20% of the Southern Hemisphere (SH). Higher surface albedo and aerosol loading in the NH make clear-sky reflection greater there than in the SH, by 6 W m^{-2} in the hemispheric mean (Voigt et al. 2013). On the other hand, the SH is cloudier than the NH (Stubenrauch et al. 2013). As it turns out, the hemispheric asymmetry in clear-sky reflection is precisely canceled by greater reflection from clouds in the SH (Stephens et al. 2015; Jönsson and Bender 2021). Further analysis of the cloud albedo asymmetry shows that it mostly arises over the extratropical oceans (Bender et al. 2017): cloud albedo averaged over the 0°–30° latitude band is very similar in the two hemispheres, so most of the asymmetry is concentrated in the

---

extratropics, while average cloud albedo over land and sea ice is almost identical in the two hemispheres, implying that the cloud albedo asymmetry is due to extratropical oceanic clouds (Datseris and Stevens 2021).

These prior results raise the fundamental question of whether the precise compensation between clear-sky and cloud albedo asymmetries is fortuitous or if it is enforced by a feedback mechanism that keeps planetary albedo symmetric (Voigt et al. 2013; Datseris and Stevens 2021). Experiments with an idealized model (Voigt et al. 2014) show that imposed asymmetries in surface albedo are compensated by a shift of the intertropical convergence zone and its attendant clouds into the darker hemisphere, raising its planetary albedo, although this reliance on tropical compensation is at odds with the major role played by extratropical asymmetries in observations. A robust feedback mechanism involving extratropical clouds remains to be identified.

Developing a comprehensive theory for planetary albedo symmetry, which would likely involve related symmetries in energy and water balances mediated by interhemispheric energy transports (Stephens et al. 2016), remains a major challenge for climate science. Our aim here is not to tackle this challenge head-on. We focus instead on a narrower question: what are the proximate causes—specifically, the local environmental conditions—that make the extratropical oceans cloudier in the SH than in the NH? Answering this question can be seen as a first step toward building a theory for the ultimate causes of planetary albedo symmetry. The answer to this question can point to some of the large-scale physical processes that such an ultimate theory should consider. Furthermore, climate models fail to robustly capture the observed planetary albedo symmetry (Voigt et al. 2013; Jönsson and Bender 2021), and insight into the physical processes controlling cloud albedo asymmetry could help correct these biases and improve cloud representation in models.

Clouds respond strongly to the dynamics and thermodynamics of the environment in which they form, and a substantial literature exists connecting cloudiness to specific environmental metrics such as low-level stability or vertical velocity, collectively referred to as "cloud-controlling factors" (CCFs; Stevens and Brenguier 2009; Klein et al. 2017). CCFs can be used to statistically explain cloud changes following a two-step approach. First, the sensitivity of clouds to a specified set of CCFs is observationally quantified, typically by multiple linear regression. Second, the change in cloudiness between two climate states can be predicted given knowledge of the corresponding change in the CCFs. Additionally, the sensitivity, together with the magnitude of the change in a given CCF, can be used to diagnose how much that CCF contributes to the total cloud change. This approach has been widely applied to analyze cloud feedbacks in future simulated climates (Zelinka et al. 2020; Ceppi and Nowack 2021; Myers et al. 2021). Here we apply it instead to understand climatological cloud differences between two regions—the extratropical oceans of the NH and SH—in the current climate. Our main aim is to identify CCFs whose hemispheric asymmetry can best explain the asymmetry in oceanic cloud albedo, and thus tie the asymmetry to specific physical mechanisms.

As detailed in section 2, we use daily MODIS satellite retrievals to characterize clouds, and ERA5 data for the cloud-controlling factors. Section 3 presents the climatology of MODIS cloud observations and shows that the hemispheric asymmetry in cloud albedo is indeed concentrated in the extratropics. Section 4 lays out our CCF methodology, and in section 5 we apply this framework to a set of six CCFs. We find a leading role for two of them—surface wind and sea surface temperature—in explaining the hemispheric cloud albedo asymmetry. Section 6 explores the local- and global-scale physical mechanisms relevant to these two CCFs, while section 7 summarizes our conclusions.

2. Data

To characterize cloud properties, we use shortwave cloud optical thickness, cloud fraction, and cloud-top pressure retrievals from the Moderate Resolution Imaging Spectroradiometer (MODIS), specifically the Level-3 daily-mean product on a global 1° grid for the period 2003–17 (King et al. 1992; Platnick et al. 2003; King et al. 2003; Hubanks et al. 2020).

The limitations of MODIS cloud products have been extensively studied (Marchand et al. 2010; Pincus et al. 2012; Grosvenor and Wood 2014; Khanal and Wang 2018) and we briefly comment on the aspects most relevant to our work. An important source of uncertainty arises from MODIS viewing only the highest cloud tops; the retrieved cloud phase and particle size from above are assumed to be uniform throughout the cloud. Also, MODIS cannot detect liquid cloud below moderately thick ice cloud. Further, MODIS produces two cloud fraction estimates: "mask cloud fractional cover," which counts the proportion of pixels deemed by the algorithm to be cloudy or probably cloudy, and "retrieval cloud fractional cover," which counts the proportion of available pixels for which cloud optical properties are successfully retrieved. The latter is a more conservative metric, and its values are on average ~10% lower than those of the former at the same grid point (and in some subtropical regions the difference exceeds 20%). The results presented here use mask cloud fractional cover, but we have verified that using retrieval cloud fractional cover does not qualitatively change our results and conclusions.

In addition, the gridded daily Level-3 product is obtained by averaging many subdaily observations in each grid cell. Since we are interested in the cloud optical thickness as a means to characterize cloud albedo (see section 3), we use the "radiatively effective" cloud optical thickness product obtained by logarithmically averaging individual observations. As argued in Pincus et al. (2012), this is preferable for applications where cloud-radiative interaction is the focus because of the near-linearity of cloud albedo as a function of the logarithm of cloud optical thickness. Linear averaging would bias the mean cloud optical thickness toward low values and yield an underestimate of cloud albedo.

Cloud-controlling factors are computed from the ERA5 product (Hersbach et al. 2020). Variables are averaged to daily means and spatially regridded to match the MODIS cloud data. We consider six primary CCFs: sea surface temperature SST (but

note that where sea ice is present we take the skin temperature of the sea ice); estimated inversion strength (EIS), defined as in Wood and Bretherton (2006) and using a constant near-surface relative humidity of 80% to compute the lifting condensation level (McCoy et al. 2017); midtropospheric pressure velocity ω_{500}; atmosphere–ocean surface temperature difference $\Delta T_{\text{sfc}} = \text{SST} - T_{2\text{m}}$; surface wind speed $V_{\text{sfc}} = (u_{10\text{m}}^2 + v_{10\text{m}}^2)^{1/2}$; and the marine cold-air outbreak index (MCAO) defined as MCAO $= \theta_{\text{SST}} - \theta_{800}$, where θ_{SST} and θ_{800} are the potential temperatures at the surface and 800 hPa respectively (Fletcher et al. 2016). We additionally consider three further CCFs: surface temperature advection $\text{AdvT}_{\text{sfc}} = -\mathbf{u}_{10\text{m}} \cdot \nabla\text{SST}$; surface latent heat flux defined through the bulk aerodynamic formula $Q_{\text{LH}} = \rho V_{\text{sfc}} C_D (q_{\text{sfc}} - q_{2\text{m}})$; and the near-surface relative humidity $\text{RH}_{2\text{m}}$.

3. Cloud climatology and albedo asymmetry

While most previous studies investigating environmental controls on clouds or shortwave reflection have focused on cloud fraction or cloud optical thickness responses separately, here we follow previous work (Datseris and Stevens 2021) and tie these two parameters together into a cloud albedo C defined as

$$C = f \frac{\sqrt{3}(1 - g)\tau}{2 + \sqrt{3}(1 - g)\tau}, \tag{1}$$

where τ is radiatively effective cloud optical thickness (hereinafter referred to as cloud optical thickness for brevity), f is cloud fraction, and g is an asymmetry factor from the cloud particle phase function. In this approach, cloud albedo is an intrinsic property of clouds, and independent of incident shortwave radiation. As shown in Datseris and Stevens (2021), g has very weak spatial variability, so for simplicity we set $g = 0.91$, which is the global-mean value calculated in that paper.

Figure 1 presents the climatological zonal-mean C, cloud fraction, and cloud optical thickness for the two hemispheres. As discussed in the introduction, previous work shows that the relevant cloud albedo asymmetry—which compensates for clear-sky albedo asymmetry rendering planetary albedo symmetric—is concentrated over the oceans, so we focus here and in the rest of the paper on oceanic regions only. The global-mean area-weighted oceanic cloud albedo comes to 0.24, and the hemispheric cloud albedo asymmetry (i.e., the hemispheric mean of the SH−NH difference shown by the black line in Fig. 1a) comes to 0.03. SH oceanic clouds are therefore around 0.03/0.24 = 12.5% brighter than their NH counterparts. The product of climatological zonal-mean C by annual-mean insolation at each latitude averaged over the hemisphere provides a rough estimate of the solar radiation reflected by clouds; this estimate indicates a hemispheric asymmetry of around 5 W m^{-2} in radiation reflected by oceanic clouds, very close to the ~6 W m^{-2} asymmetry in observed clear-sky reflection (Voigt et al. 2013).

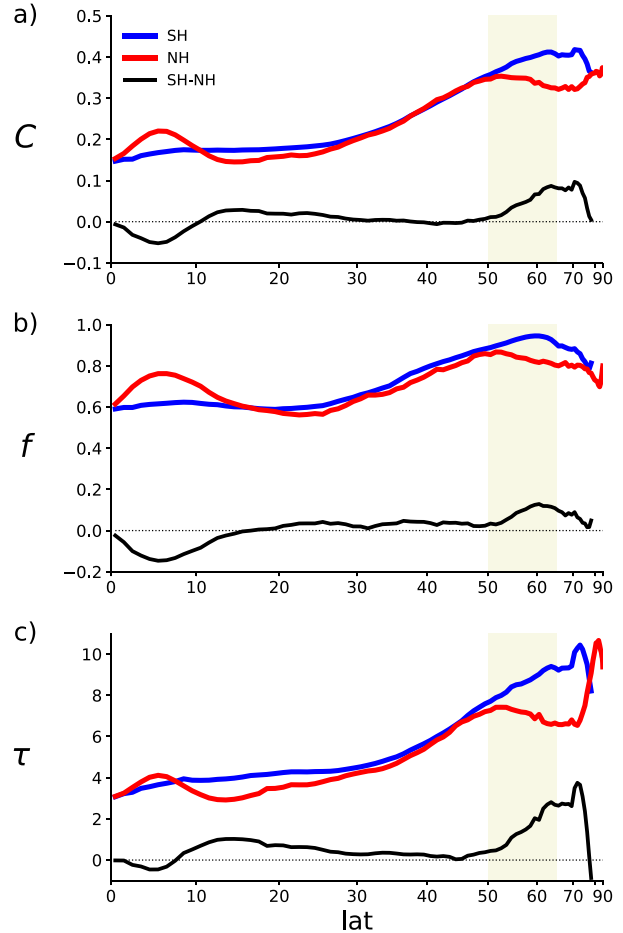Cloud albedo differs between the two hemispheres both in the tropics and in the middle to high latitudes. However,

FIG. 1. Annual- and zonal-mean (a) cloud albedo C, (b) cloud fraction f, and (c) cloud optical thickness τ. Averages are computed over oceans only. Red lines indicate the NH, blue lines the SH, and black lines the SH − NH difference. Light shading indicates the 50°–65° latitude band.

the hemispheric cloud albedo asymmetry averaged between 0° and 30° is very small (around 0.5% of the global mean), which implies that almost the entire hemispheric cloud albedo asymmetry comes from the extratropics, in particular from the region poleward of around 50° latitude. Since winter data is largely missing from the satellite retrievals poleward of the polar circle (66.6° latitude), and since these regions are mostly land (especially in the SH), we restrict attention to the 50°–65° band.

Thus, the remainder of this study is focused on the extratropical cloud albedo asymmetry $\Delta\overline{C}$ defined as

$$\Delta\overline{C} = \overline{C}_S - \overline{C}_N, \tag{2}$$

where overbars indicate climatological annual averages over the oceanic portions of the 50°–65° latitude band, while subscripts N and S refer to the NH and SH respectively (area-weighting is applied to meridional averages, i.e., multiplied by cosine of latitude). Numerically, we find $\overline{C}_S = 0.39$, $\overline{C}_N = 0.34$, and $\Delta\overline{C} = 0.05$.

4. Cloud-controlling factor framework

Our goal here is to quantify the fraction of the extratropical cloud albedo asymmetry $\Delta\overline{C}$ (section 3) that is statistically explained (or predicted) by hemispheric asymmetry in one or more CCFs. We use an approach similar to that of Bony et al. (2004), which avoids the use of linear regression and thus incorporates the full, generally nonlinear response of clouds to their controlling factors. For ease of notation, we present the methodology for the case where a single CCF, denoted x, is used to predict $\Delta\overline{C}$.

We first define the *response functions* $C_N(x)$ and $C_S(x)$, which give the expected value of cloud albedo for a given value of the controlling factor x (i.e., the conditionally averaged cloud albedo) in the NH and SH respectively. These response functions are estimated in practice by binning cloud albedo values at each day and grid point by the value of x at the same time and grid point, and then averaging within each bin; these bin averages include data from all days in the 15-yr period and all grid points in the oceanic portions of the 50°–65° latitude band in each hemisphere, using area weighting. We use 40 equispaced bins spanning the range of x. Note that we retain the full daily variability of clouds and CCFs, since we expect synoptic-scale processes to be important in this latitude range (Kelleher and Grise 2019).

Given the response functions, the climatological cloud albedo asymmetry (2) can be written as

$$\Delta\overline{C} = \int \left[C_S(x)\, P_S(x) - C_N(x)\, P_N(x) \right] dx, \qquad (3)$$

where $P_N(x)$ and $P_S(x)$ are the probability density functions (PDFs) of x in the oceanic 50°–65° latitude band of the NH and SH respectively, estimated as area-weighted normalized histograms over the same bins used to compute the response functions. To interpret (3), consider two limiting cases. In one limit, $C_S(x) = C_N(x)$ while $P_S(x) \neq P_N(x)$; in this case x has perfect skill in the sense that the entire cloud albedo asymmetry is predicted by interhemispheric differences in the PDF of x. In the opposite limit, $C_S(x) \neq C_N(x)$ while $P_S(x) = P_N(x)$, in which case x is perfectly unskilled since it explains none of the albedo asymmetry. Cloud properties are in fact simultaneously determined by myriad different environmental factors. For a given value of x, all the other factors will generally have different values in the two hemispheres (more precisely, the joint PDF of all other CCFs conditional on x will be different in the two hemispheres). It is the asymmetry in other CCFs that makes $C_S(x) \neq C_N(x)$. Therefore, in this second limit, the albedo asymmetry is entirely explained by asymmetries in CCFs *other* than x.

Real situations will be intermediate between these two limits, with a fraction of $\Delta\overline{C}$ explained by x and the remainder by other CCFs. To quantify these contributions, we rewrite (3) identically as

$$\Delta\overline{C} = \underbrace{\frac{1}{2}\int (C_S + C_N)(P_S - P_N)dx}_{\Delta\overline{C}_A} + \underbrace{\frac{1}{2}\int (C_S - C_N)(P_S + P_N)dx}_{\Delta\overline{C}_B}$$

$$\qquad (4)$$

and define

$$A = \frac{\Delta\overline{C}_A}{\Delta\overline{C}}, \qquad (5)$$

where $\Delta\overline{C}_A$ is the first term on the r.h.s. of (4). The ratio A captures the fraction of $\Delta\overline{C}$ attributable to hemispheric asymmetry in the PDF of x, and is thus a measure of x's skill in predicting the total albedo asymmetry $\Delta\overline{C}$. The residual $B = 1 - A = \Delta\overline{C}_B / \Delta\overline{C}$ can be interpreted as the fraction of $\Delta\overline{C}$ explained by CCFs other than x. Note that A is not constrained to lie between 0 and 1; $A < 0$ means that x predicts albedo asymmetry in the opposite direction to that observed (i.e., it predicts a brighter NH), while $A > 1$ means that x predicts a very bright SH which is made darker by other CCFs. We calculate A in practice by numerically computing the integral in $\Delta\overline{C}_A$ using the trapezoidal approximation for better accuracy. To facilitate the interpretation of these scores in connection with the P and C distributions for each hemisphere, some examples are provided in the appendix, useful for comparison with actual results from section 5.

The framework can be straightforwardly generalized to the case where several CCFs are simultaneously used to predict $\Delta\overline{C}$, with the only difference that the response functions are then defined over a multidimensional space (and their estimation requires multidimensional binning). The more common approach to estimating cloud responses to CCFs is via linear regression (Klein et al. 2017). This is equivalent in our framework to replacing the full response functions in (3) with linear regression lines. As shown in the next section, the response functions are generally nonlinear and even nonmonotonic, which would imply possibly large errors in the calculation of the skill score A with a linear approximation.

5. Predicting cloud albedo asymmetry using CCFs

We apply the above framework to our set of six primary CCFs (SST, ω_{500}, EIS, ΔT_{sfc}, V_{sfc}, and MCAO; see section 2), aiming to assess how skillfully they individually predict the observed hemispheric cloud albedo asymmetry. The first five CCFs have been widely employed in previous work and are understood to influence cloudiness through physically plausible mechanisms. Their selection here is guided by known or potential hemispheric asymmetries in their climatology. In particular, annual-mean SST is colder and surface winds stronger over the Southern Ocean than at the same latitude in the NH oceans (Scott et al. 2020). Furthermore, the SH storm track is stronger in the annual mean than its NH oceanic counterparts (O'Gorman 2010); to the extent that midlatitude storms control the variability of vertical velocity and horizontal winds, we may expect differences in the PDFs of daily ω_{500}, V_{sfc}, and also ΔT_{sfc}, which can be taken as a proxy for near-surface temperature advection. The inclusion of MCAO in our analysis is motivated by our focus on the mid- to high-latitude (50°–65°) oceans, which are characterized by frequent incursions of polar air masses for which the MCAO index was specifically developed.
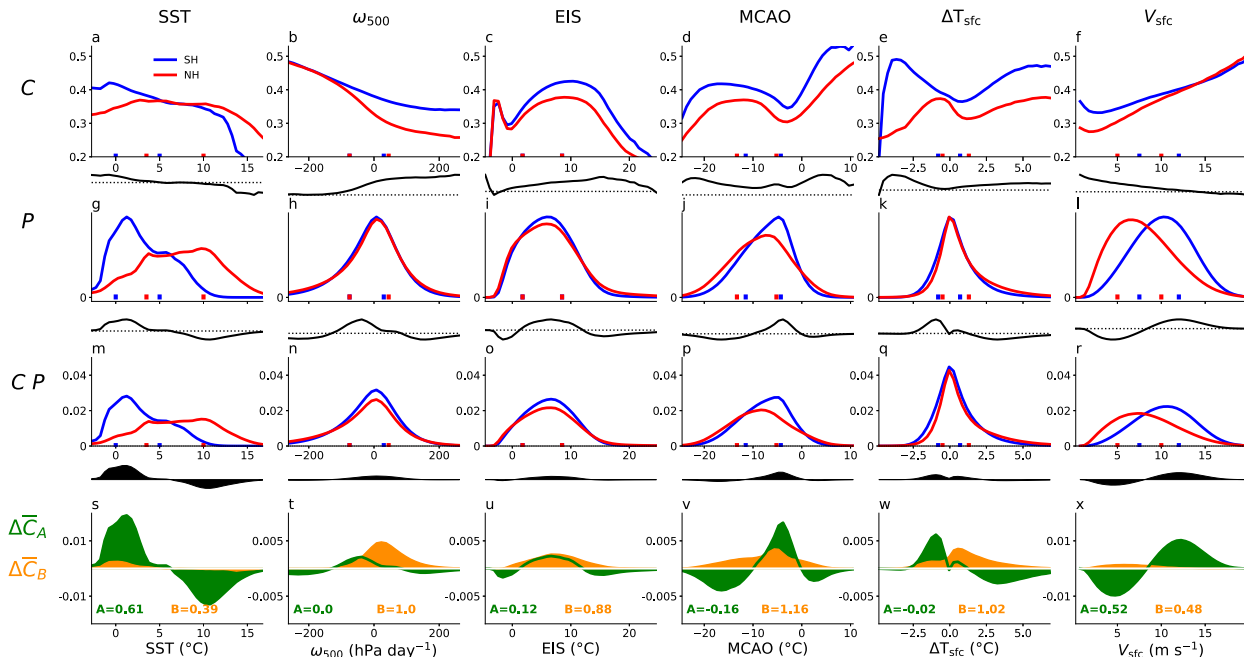
FIG. 2. (top) Cloud albedo response functions (*C*) for six CCFs as indicated above each column, and (second row) probability density functions (*P*) of the CCFs; black curves show the SH–NH difference. (third row) Product of the response and probability density functions; the black area under the difference curve is $\Delta \overline{C} = 0.05$. Small squares over the *x* axis in the top three rows indicate the interquartile range for each CCF and hemisphere (see Table 1). (bottom) Asymmetry components $\Delta \overline{C}_A$ (green) and $\Delta \overline{C}_B$ (orange) with their associated scores *A* and *B*, following Eqs. (3) and (4); note the different scale of the *y* axis. Only ocean points in 50°–65° latitude band of the NH (red) and SH (blue) are included.

Figure 2 (top row) shows the cloud albedo response functions for each of the six CCFs. The response functions are generally strongly nonlinear over the range of their CCF. The sensitivity of cloud albedo to each CCF can be quantified as the change in the response functions across the interquartile range (25th–75th percentiles) of the corresponding PDF. The results (Table 1) show that cloud albedo changes by 0.03–0.09 across this range for all CCFs in both hemispheres, with SST at the NH as the sole exception (we have also verified that linear regression coefficients scaled by standard deviation of the CCF show a similar range of sensitivity). Recalling that the total cloud albedo asymmetry $\Delta \overline{C}$ is 0.05 (section 3), it appears that a strong interhemispheric shift in the PDF of any of the CCFs could potentially explain a substantial fraction of the total. However, the middle row of Fig. 2 shows that only two of the CCFs—namely SST and V_{sfc}—exhibit an appreciable shift in the PDF. As a result, they also show the highest skill scores,

predicting 61% and 52% of the total asymmetry respectively (Table 1). The other CCFs show more subtle PDF asymmetries; in the case of EIS, this is sufficient to yield $A = 0.12$, making it the third most skillful predictor. For ω_{500}, $\Delta \overline{C}$ is due purely to the *B* component (i.e., $A = 0$); hence this CCF predicts none of the asymmetry. The remaining two CCFs (ΔT_{sfc} and MCAO) show PDF asymmetries in the opposite direction—that is, they yield $A < 0$ and predict brighter clouds in the NH than in the SH.

For a clearer interpretation of these skill scores, it is helpful to compare the behavior of the *C* and *P* curves in Fig. 2 with the idealized examples shown in appendix A. For instance, MCAO has a negative score as in case 7 (Fig. A1), and in both the peak of P_S is shifted toward lower values of cloud albedo as compared with P_N, implying that this CCF predicts lower albedo in the SH than in the NH (i.e., a negative asymmetry). Were the interhemispheric shift in PDF more

TABLE 1. Change in the cloud albedo response functions shown in Fig. 2 across the interquartile range (IQR) of the corresponding cloud-controlling factor (i.e., the change from the 25th to the 75th percentiles of the CCF's PDF) for the SH (C_S) and NH (C_N). The bottom row shows the fraction of the total cloud albedo asymmetry explained by each individual CCF [see Eq. (5)].

	SST	ω_{500}	EIS	MCAO	ΔT_{sfc}	V_{sfc}
Change in C_S over IQR	−0.048	−0.039	0.071	−0.056	−0.028	0.034
Change in C_N over IQR	−0.008	−0.088	0.050	−0.059	−0.057	0.067
A	0.61	0.00	0.12	−0.16	−0.02	0.52

pronounced, a more negative A score would obtain. Further, results for ω_{500} and ΔT_{sfc} resemble case 6 in appendix A, in which the P_S and P_N are nearly identical, yielding $A \sim 0$. On the other hand, and as noted above, the distinct shift in PDF curves for SST and V_{sfc} is similar to case 3, with $A > 50\%$.

It is noteworthy that while SST and V_{sfc} are both skilled in predicting the asymmetry, ΔT_{sfc}, which is related to near-surface temperature advection, is not. Consistently, repeating the analysis directly using surface temperature advection $AdvT_{sfc}$ as a CCF yields a score $A = 0.02$. Surface wind is also directly related to latent heat flux Q_{LH} (see section 2), but applying the method to this CCF shows it is a very poor predictor of the asymmetry ($A = 0.01$). The same is true of near-surface relative humidity RH_{2m} ($A = 0.05$).

While previous studies generally agree on the importance of SST in controlling cloudiness, the significant role played by V_{sfc} in our results is more striking since this CCF is generally found to be of lesser importance. For example, Scott et al. (2020) regressed monthly anomalies of various atmospheric controls to monthly anomalies of low clouds and radiative fluxes over the global oceans, and found that for midlatitudes the sensitivity of V_{sfc} is much smaller than for other predictors. Similar results were obtained by Grise and Kelleher (2021): the total variance of low-cloud radiative response explained by multiple linear regression onto four CCFs did not significantly increase with the incorporation of V_{sfc} as a fifth one. This difference from our results is likely due in part to that fact that we use a daily time scale that captures synoptic variability that cannot be represented with monthly data. In any case, had those studies used daily anomalies and obtained similar results, there would still be no inherent contradiction: even if V_{sfc} does not dominate midlatitude cloud variability or cloud responses to radiative forcing, it can nevertheless play an important role in setting the hemispheric cloud albedo asymmetry because of the very different midlatitude surface wind climatologies in the two hemispheres. Conversely, while ω_{500} appears as a robust CCF in our results (in the sense that cloud albedo is strongly sensitive to ω_{500} in both hemispheres; Fig. 2b), it is nonetheless a very poor predictor of the hemispheric cloud albedo asymmetry because its PDF is nearly identical in both hemispheres.

To assess the sensitivity of our results to the dataset used to compute CCFs, we recalculate all results using the ERA-Interim reanalysis product (Dee et al. 2011), the predecessor of ERA5. The equivalents of Table 1 and Fig. 2 produced with this dataset can be found in appendix B. Overall differences are small, except for a considerably smaller skill score for SST in the ERA-Interim product ($A = 0.24$) than in ERA5 ($A = 0.61$). This difference can be traced to the different behavior of C_S at the upper end of the SST distribution in the two datasets: ERA5 indicates much smaller values of SH cloud albedo at SST $> 10°C$ than ERA-Interim (cf. Figs. 2a and B1a). ERA5 also has a lower frequency of SST $> 10°C$ occurrences (in fact, the annual-mean SST field in ERA-Interim is generally 1° and 2°C warmer than in ERA5 in our region of interest, and up to 3°C near the Antarctic peninsula; not shown). This sensitivity to tail events is a caveat to our CCF methodology. Nonetheless, the qualitative result that

SST and V_{sfc} are the two leading factors explaining the asymmetry remains robust.

6. Physical mechanisms

Surface wind can affect cloudiness at all levels in the troposphere through different physical mechanisms. In extratropical cyclones, stronger surface winds are associated with greater boundary layer moisture convergence and upward moisture transport along the "warm conveyor belt" structure linking the boundary layer to upper levels, producing greater mid- and high-level cloudiness (Field and Wood 2007; McCoy et al. 2019). Surface wind also affects surface turbulent fluxes and thus boundary layer thermodynamics and cloudiness: large-eddy simulation studies (Nuijens and Stevens 2012; Bretherton et al. 2013; Kazil et al. 2016) show that increasing surface wind induces an adjustment of the boundary layer favoring thicker low-level clouds with greater fractional cover.

Distinguishing which of these mechanisms is most relevant here requires establishing what cloud type is most important in generating the hemispheric cloud albedo asymmetry. To do so, it is useful to examine cloud response functions to joint variations in V_{sfc} and ω_{500}, since the latter naturally sorts cloud scenes with abundant high clouds (associated with ascent) from those with predominantly low clouds (associated with subsidence).

Figure 3 shows the joint response functions for cloud albedo, cloud fraction, cloud optical thickness, and cloud top pressure (CTP). We see (Figs. 3d,h) the expected sorting of cloud type by vertical velocity, with low cloud tops under subsiding conditions and higher cloud tops with ascent irrespective of surface wind. Referring back to Fig. 2n, where the black line shows the contribution to hemispheric albedo asymmetry for each value of ω_{500}, we note that positive contributions to the asymmetry are concentrated in the range $|\omega_{500}| < 100$ hPa day^{-1}. From Figs. 3d and 3h we see in turn that this range of vertical velocities corresponds to cloud tops ~ 600–900 hPa, implicating mostly low clouds. An alternative approach is to compute mean cloud albedo stratified by CTP bins (i.e., treating CTP formally as a CCF), which shows (Fig. 4) that positive contributions to hemispheric albedo asymmetry peak at CTP ~ 700 hPa. We conclude therefore that the extratropical cloud albedo asymmetry $\Delta \overline{C}$ arises predominantly from low clouds, with some contribution from midlevel clouds.

The modeling study of Nuijens and Stevens (2012) makes three specific predictions for how low clouds respond to surface wind: increasing V_{sfc} should lead to greater cloud fraction, optical thickness, and cloud-top height. Figure 3 shows that all three predictions are borne out: under subsidence conditions, when low clouds prevail, stronger V_{sfc} yields greater cloud fraction (Figs. 3b,f), greater optical thickness (Figs. 3c,g), and higher cloud tops (Figs. 3d,h). The simulations of Nuijens and Stevens (2012) were designed to capture subtropical subsidence conditions, and their results have been empirically corroborated using satellite imagery from the trade wind region (Mieslinger et al. 2019). Our present results suggest that similar physics also controls low cloud responses to surface wind in extratropical oceanic regions. To make this similarity
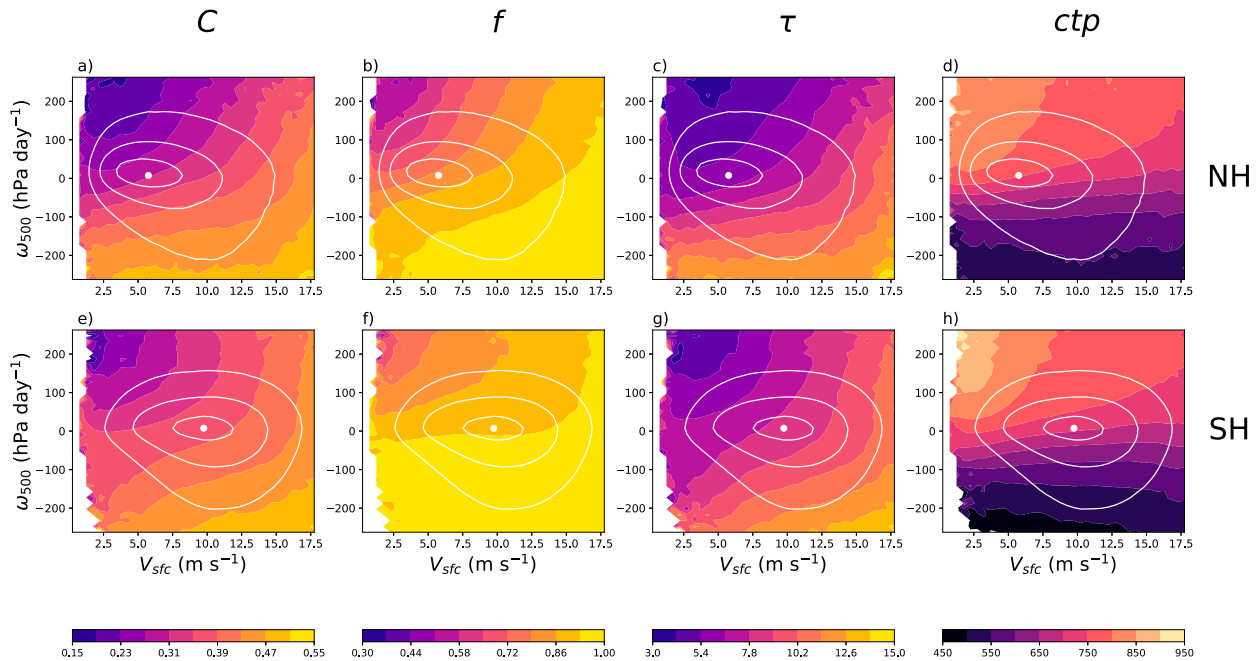
FIG. 3. Joint response functions to ω_{500} and V_{sfc} (shading) for (from left to right) cloud albedo C, cloud fraction, cloud optical thickness, and cloud-top pressure for ocean points in 50°–65° latitude band of the (top) NH and (bottom) SH. White contours show the joint ω_{500}–V_{sfc} probability density functions (contours correspond to values of 0.5, 2, and 4 of the normalized PDF × 1000) while inner white dot is the mode of the PDF.

more explicit, Fig. 5 compares surface wind response functions computed over a number of subtropical and extratropical regions; despite different mean levels of cloudiness in each region, the structure of the response functions and the sensitivity of cloud albedo to surface wind is very similar across all regions. Nonetheless, further work would be required to establish that the physical processes by which surface wind affects low-level clouds in the extratropics are in fact the same as those in the subtropical regions addressed by previous modeling work (Nuijens and Stevens 2012).

Besides surface wind, SST also explains a substantial fraction of $\Delta\overline{C}$. Our results also show that cloud albedo generally decreases with increasing SST, at least over the range of SST where the bulk of the data is concentrated (Figs. 2a,g and Table 1). This response is in agreement with previous observational evidence on the relation between low clouds and SST in both the tropics and extratropics (Bony and Dufresne 2005; Scott et al. 2020). Modeling work (Rieck et al. 2012; Bretherton and Blossey 2014) also consistently shows that colder SST favors greater low-cloud cover, although the precise mechanism remains debated.
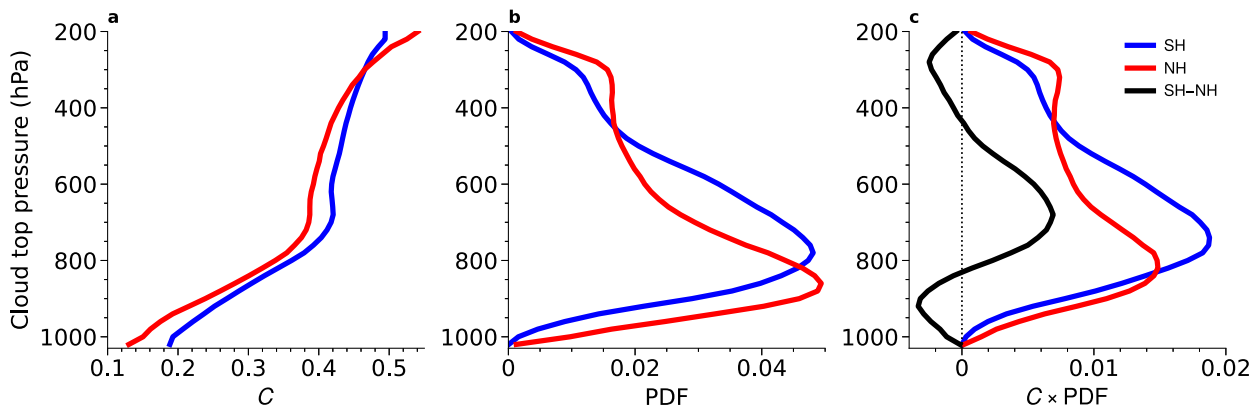

FIG. 4. (a) Cloud albedo as a function of cloud-top pressure, (b) cloud-top pressure probability density functions, and (c) the product of cloud albedo and probability density functions for ocean points in 50°–65° latitude band of the NH (red lines) and SH (blue). Black line in (c) shows the SH − NH difference.
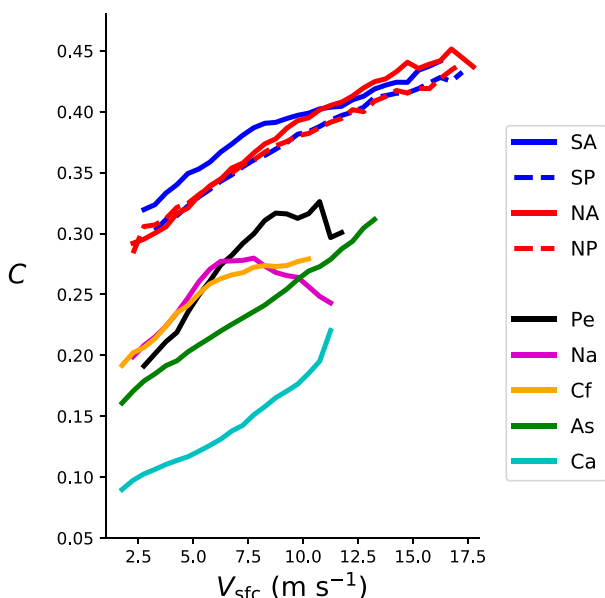
FIG. 5. Cloud albedo response functions to V_{sfc} for five subtropical stratocumulus regions, and comparison with four extratropical regions, for the 15-yr period. Subtropical region labels correspond to the Peruvian (Pe), Namibian (Na), Californian (Cf), Australian (As), and Canarian (Ca) regions. The extratropical regions are South Atlantic (SA), South Pacific (SP), North Atlantic (NA), and North Pacific (NP). All these regions are the same oceanic $10° \times 10°$ boxes specified in Wood and Bretherton (2006), except for the SP (50°–60°N, 140°–150°W) and SA (50°–60°N, 35°–45°W) cases that have been additionally incorporated into our comparison.

Computing the joint V_{sfc}–SST skill score exactly as in (5) but using joint response functions and PDFs in (4), we obtain $A = 1.20$, implying that surface wind and SST jointly explain the entire asymmetry, with an excess of 20% which must be compensated by other factors (note for example that MCAO predicts a negative asymmetry, with $A = -0.16$). Notably, the joint V_{sfc}–SST skill score is close to the sum of the corresponding single-CCF values $(0.61 + 0.52 = 1.13)$. Using the ERA-Interim dataset, the joint V_{sfc}–SST skill score is $A = 0.91$, so we can robustly conclude that V_{sfc} and SST are sufficient to predict most or all of the observed cloud albedo asymmetry.

The stronger surface winds and colder SSTs of the SH both act in the same direction, inducing local-scale boundary layer effects that make low clouds brighter there than over NH oceans. In addition, satellite imagery shows that low-level cloudiness in these regions exhibits ubiquitous mesoscale organization reminiscent of that seen in the trade-wind region, and observational studies (McCoy et al. 2017; Bony et al. 2020; Schulz et al. 2021) show that this organization strongly depends on V_{sfc} (and to a lesser extent also on SST) and is associated with systematic changes in the low-cloud fraction, with a larger low-cloud fraction and deeper clouds when V_{sfc} increases. This aspect provides an interesting avenue for future work.

The coincidence of cold SST and strong surface wind in the SH midlatitudes is not accidental, but obeys large-scale macroturbulence constraints: the colder annual-mean SST in the Southern Ocean implies larger meridional temperature gradient, greater baroclinicity, and a more active storm track than in the NH (O'Gorman 2010). Stronger midlatitude eddy activity yields stronger surface wind speeds in mid- to high latitudes both by enhancing transient surface wind variability, and also by increasing upper-level eddy momentum flux convergence, which drives stronger surface westerlies. In turn, the zonal surface wind stress drives strong oceanic ocean upwelling in the Southern Ocean (Marshall and Speer 2012), which helps keep SST cold there and strongly modulates its response to global radiative forcing (Armour et al. 2016). The coupling between local-scale cloud responses and the global-scale ocean–atmosphere general circulation outlined here opens up a variety of possible climate feedback mechanisms that would be worth exploring in future work seeking a comprehensive theory for planetary albedo symmetry.

7. Conclusions

We have studied oceanic cloud albedo—defined as in Eq. (1) and quantified using MODIS satellite retrievals—with the aim of assessing its hemispheric asymmetry and determining to what extent this asymmetry can be predicted by cloud-controlling factors independently from one another. We summarize our main conclusions as follows:

(i) Southern Hemisphere oceanic clouds as observed by MODIS are substantially brighter than their Northern Hemisphere counterparts. This hemispheric cloud albedo asymmetry is concentrated in the region poleward of 50° latitude. While tropical cloud albedo is not symmetric on a latitude-by-latitude basis, tropical averages over the 0°–30° latitude band (or the 0°–50° band) are almost perfectly symmetric.

(ii) Focusing on the 50°–65° latitude band, we find that among the several CCFs considered here SST individually predicts the largest fraction of the hemispheric cloud albedo asymmetry, followed by surface wind; these two CCFs jointly predict 120% of the asymmetry. Low-level stability as measured by EIS captures a smaller fraction of the asymmetry, while the remaining CCFs predict either no asymmetry or an asymmetry of the opposite sign (i.e., they predict brighter clouds in the NH).

(iii) Low clouds—with cloud-top pressures around 700 hPa—provide the dominant contribution to the asymmetry, with some contribution also from midlevel clouds. The low-cloud response to V_{sfc} and SST found here qualitatively agrees with previous modeling work showing that marine boundary layer clouds become optically thicker and more extensive as surface wind increases and surface temperature decreases. This agreement suggests that the proximate cause for the hemispheric cloud albedo asymmetry are the local boundary layer effects of the Southern Ocean's cooler SSTs and
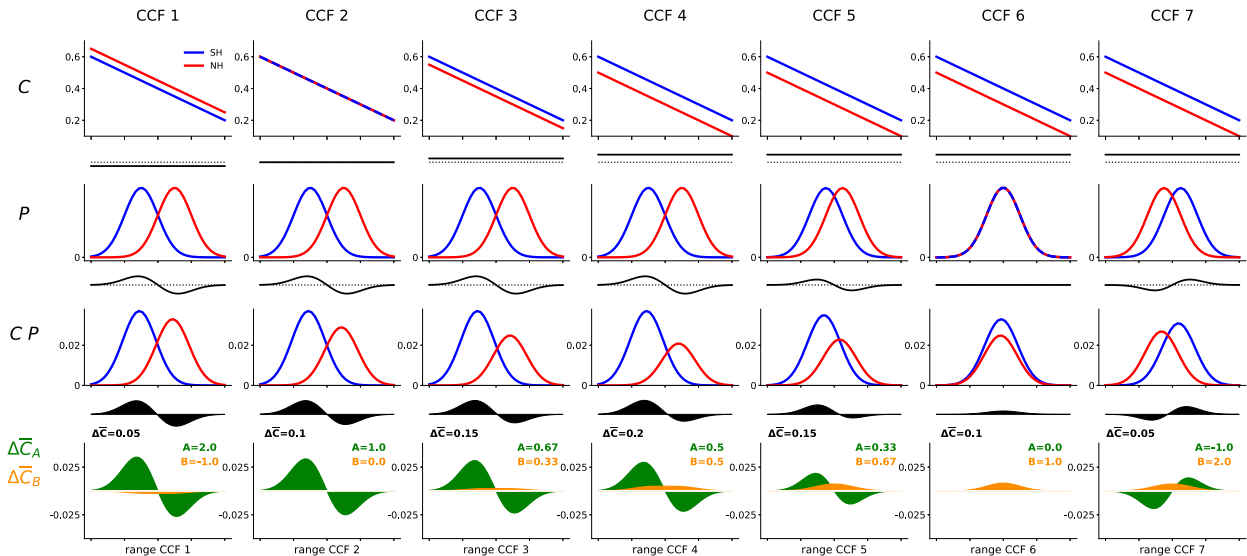
FIG. A1. (from top to bottom) Cloud albedo response functions (C), probability density functions (P), their product for each hemisphere, and total asymmetry $\Delta\overline{C}$ and its A and B components for seven toy examples of CCF. Black curves show the SH − NH difference. For simplicity, the same Gaussian distribution for P is taken with changes only to the mean, while the same linear function is taken for C, with changes only to the intercept. The P_S and P_N distributions are identical across cases 1–4, while C_S and C_N are identical across cases 4–7. Notice that the value of asymmetry $\Delta\overline{C}$ may change from case to case.

stronger surface winds as compared with oceans at similar latitudes in the NH.

From a general circulation perspective, cooler SSTs entail a stronger equator–pole temperature gradient, greater overall baroclinicity and a more intense storm track. The combination of strong local-scale control of low clouds by V_{sfc} and SST together with large-scale coupling of surface wind and SST gradients opens up a rich array of possibilities for climate feedbacks over multiple time scales, coupling local cloud changes to the general circulation of the atmosphere and ocean. Further investigation of these possible implications could help pave the way to a theory of global planetary albedo and its symmetry.

Data availability statement. The datasets used this work were obtained from the ERA5 and ERA-Interim and MODIS COSP L3 online repositories at https://www.ecmwf.int/en/forecasts/datasets/reanalysis-datasets/era-interim, https://www. ecmwf.int/en/forecasts/datasets/reanalysis-datasets/era5, and https://ladsweb.modaps.eosdis.nasa.gov/missions-and-measurements/products/MCD06COSP_D3_MODIS, respectively.

APPENDIX A

Idealized Skill Score Examples

Figure A1 shows seven idealized cases of hemispheric albedo asymmetry (brighter SH) in which the A score ranges from overpredicting the asymmetry ($A > 1$, CCF1) to predicting a brighter NH, that is, a negative asymmetry ($A < 0$, CCF 7). CCF2 is a perfectly skilled predictor of the asymmetry, $A = 1$, while CCF6 is perfectly unskilled, $A = 0$. CCFs 1 and 3 can be regarded as good predictors of the asymmetry given that the PDF for the SH peaks at higher cloud albedo values than in the NH, while the albedo response functions are very similar.

APPENDIX B

Results with ERA-Interim

Here we present the same results as in the main text but obtained using ERA-Interim instead of ERA5 data. The

TABLE B1. As in Table 1, but for ERA-Interim.

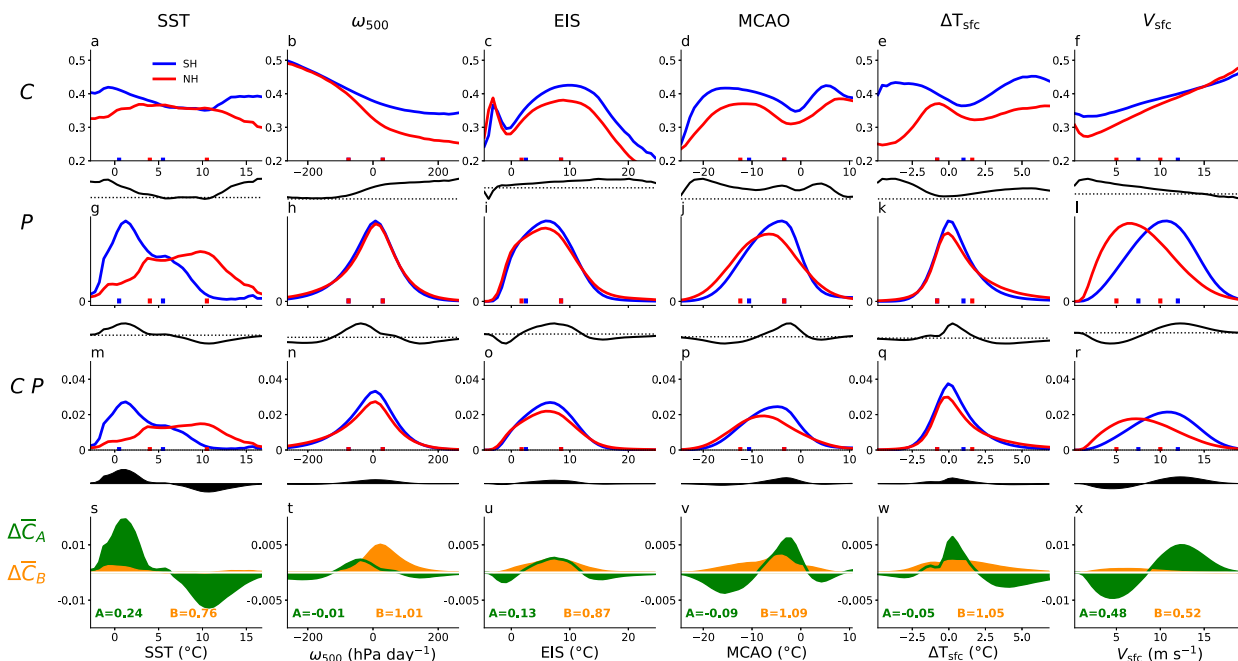|	SST	ω_{500}	EIS	MCAO	ΔT_{sfc}	V_{sfc}
Change in C_S over IQR	−0.047	−0.043	0.058	−0.044	−0.031	0.031
Change in C_N over IQR	−0.009	−0.089	0.056	−0.058	−0.049	0.060
A	0.24	−0.01	0.13	−0.09	−0.05	0.48

FIG. B1. As in Fig. 2 but for ERA-Interim.

joint V_{sfc}–SST skill score using ERA-Interim data is $A = 0.91$. Results for the single-CCF analysis are shown in Table B1 and Fig. B1.

REFERENCES

Armour, K. C., J. Marshall, J. R. Scott, A. Donohoe, and E. R. Newsom, 2016: Southern Ocean warming delayed by circumpolar upwelling and equatorward transport. *Nat. Geosci.*, **9**, 549–554, https://doi.org/10.1038/ngeo2731.

Bender, F. A.-M., A. Engström, R. Wood, and R. J. Charlson, 2017: Evaluation of hemispheric asymmetries in marine cloud radiative properties. *J. Climate*, **30**, 4131–4147, https://doi.org/10.1175/JCLI-D-16-0263.1.

Bodas-Salcedo, A., K. D. Williams, P. R. Field, and A. P. Lock, 2012: The surface downwelling solar radiation surplus over the Southern Ocean in the Met Office Model: The role of midlatitude cyclone clouds. *J. Climate*, **25**, 7467–7486, https://doi.org/10.1175/JCLI-D-11-00702.1.

——, and Coauthors, 2014: Origins, of the solar radiation biases over the Southern Ocean in CFMIP2 models. *J. Climate*, **27**, 41–56, https://doi.org/10.1175/JCLI-D-13-00169.1.

——, P. G. Hill, K. Furtado, K. D. Williams, P. R. Field, J. C. Manners, P. Hyder, and S. Kato, 2016: Large contribution of supercooled liquid clouds to the solar radiation budget of the Southern Ocean. *J. Climate*, **29**, 4213–4228, https://doi.org/10.1175/JCLI-D-15-0564.1.

Bony, S., and J.-L. Dufresne, 2005: Marine boundary layer clouds at the heart of tropical cloud feedback uncertainties in climate models. *Geophys. Res. Lett.*, **32**, L20806, https://doi.org/10.1029/2005GL023851.

——, ——, H. Le Treut, J.-J. Morcrette, and C. Senior, 2004: On dynamic and thermodynamic components of cloud changes.

Climate Dyn., **22**, 71–86, https://doi.org/10.1007/s00382-003-0369-6.

——, H. Schulz, J. Vial, and B. Stevens, 2020: Sugar, gravel, fish, and flowers: Dependence of mesoscale patterns of trade-wind clouds on environmental conditions. *Geophys. Res. Lett.*, **47**, e2019GL085988, https://doi.org/10.1029/2019GL085988.

Bretherton, C. S., and P. N. Blossey, 2014: Low cloud reduction in a greenhouse-warmed climate: Results from Lagrangian LES of a subtropical marine cloudiness transition. *J. Adv. Model. Earth Syst.*, **6**, 91–114, https://doi.org/10.1002/2013MS000250.

——, ——, and C. R. Jones, 2013: Mechanisms of marine low cloud sensitivity to idealized climate perturbations: A single-LES exploration extending the CGILS cases. *J. Adv. Model. Earth Syst.*, **5**, 316–337, https://doi.org/10.1002/jame.20019.

Ceppi, P., and P. Nowack, 2021: Observational evidence that cloud feedback amplifies global warming. *Proc. Natl. Acad. Sci. USA*, **118**, e2026290118, https://doi.org/10.1073/pnas.2026290118.

Datseris, G., and B. Stevens, 2021: Earth's albedo and its symmetry. *AGU Adv.*, **2**, e2021AV000440, https://doi.org/10.1029/2021AV000440.

Dee, D. P., and Coauthors, 2011: The ERA-Interim reanalysis: Configuration and performance of the data assimilation system. *Quart. J. Roy. Meteor. Soc.*, **137**, 553–597, https://doi.org/10.1002/qj.828.

Field, P. R., and R. Wood, 2007: Precipitation and cloud structure in midlatitude cyclones. *J. Climate*, **20**, 233–254, https://doi.org/10.1175/JCLI3998.1.

Fletcher, J., S. Mason, and C. Jakob, 2016: The climatology, meteorology, and boundary layer structure of marine cold air outbreaks in both hemispheres. *J. Climate*, **29**, 1999–2014, https://doi.org/10.1175/JCLI-D-15-0268.1.

Grise, K. M., and M. K. Kelleher, 2021: Midlatitude cloud radiative effect sensitivity to cloud controlling factors in observations and models: Relationship with Southern Hemisphere

jet shifts and climate sensitivity. *J. Climate*, **34**, 5869–5886, https://doi.org/10.1175/JCLI-D-20-0986.1.

Grosvenor, D. P., and R. Wood, 2014: The effect of solar zenith angle on MODIS cloud optical and microphysical retrievals within marine liquid water clouds. *Atmos. Chem. Phys.*, **14**, 7291–7321, https://doi.org/10.5194/acp-14-7291-2014.

Haynes, J. M., C. Jakob, W. B. Rossow, G. Tselioudis, and J. Brown, 2011: Major characteristics of Southern Ocean cloud regimes and their effects on the energy budget. *J. Climate*, **24**, 5061–5080, https://doi.org/10.1175/2011JCLI4052.1.

Hersbach, H., and Coauthors, 2020: The ERA5 global reanalysis. *Quart. J. Roy. Meteor. Soc.*, **146**, 1999–2049, https://doi.org/10.1002/qj.3803.

Houze, R. A., 2014: *Cloud Dynamics*. International Geophysics Series, Vol. 104, Academic Press, 432 pp.

Hubanks, P., R. Pincus, S. Platnick, and K. Meyer, 2020: Level-3 MCD06 COSP cloud properties user guide. NASA MODIS Adaptive Processing System, Goddard Space Flight Center, 110 pp.

IPCC, 2013: *Climate Change 2013: The Physical Science Basis*. Cambridge University Press, 1535 pp.

Jönsson, A., and F. A.-M. Bender, 2021: Persistence and variability of Earth's interhemispheric albedo symmetry in 19 years of CERES EBAF observations. *J. Climate*, **35**, 249–268, https://doi.org/10.1175/JCLI-D-20-0970.1.

Kazil, J., G. Feingold, and T. Yamaguchi, 2016: Wind speed response of marine non-precipitating stratocumulus clouds over a diurnal cycle in cloud-system resolving simulations. *Atmos. Chem. Phys.*, **16**, 5811–5839, https://doi.org/10.5194/acp-16-5811-2016.

Kelleher, M. K., and K. M. Grise, 2019: Examining Southern Ocean cloud controlling factors on daily time scales and their connections to midlatitude weather systems. *J. Climate*, **32**, 5145–5160, https://doi.org/10.1175/JCLI-D-18-0840.1.

Khanal, S., and Z. Wang, 2018: Uncertainties in MODIS-based cloud liquid water path retrievals at high latitudes due to mixed-phase clouds and cloud top height inhomogeneity. *J. Geophys. Res. Atmos.*, **123**, 11 154–11 172, https://doi.org/10.1029/2018JD028558.

King, M. D., Y. J. Kaufman, W. P. Menzel, and D. Tanre, 1992: Remote sensing of cloud, aerosol, and water vapour properties from the Moderate Resolution Imaging Spectrometer (MODIS). *IEEE Trans. Geosci. Remote Sens.*, **30**, 2–27, https://doi.org/10.1109/36.124212.

——, and Coauthors, 2003: Cloud and aerosol properties, precipitable water, and profiles of temperature and water vapor from MODIS. *IEEE Trans. Geosci. Remote Sens.*, **41**, 442–458, https://doi.org/10.1109/TGRS.2002.808226.

Klein, S. A., A. Hall, J. R. Norris, and R. Pincus, 2017: Low-cloud feedbacks from cloud-controlling factors: A review. *Surv. Geophys.*, **38**, 1307–1329, https://doi.org/10.1007/s10712-017-9433-3.

Marchand, R., T. Ackerman, M. Smythe, and W. B. Rossow, 2010: A review of cloud top height and optical depth histograms from MISR, ISCCP and MODIS. *J. Geophys. Res.*, **115**, D16206, https://doi.org/10.1029/2009JD013422.

Marshall, J., and K. Speer, 2012: Closure of the meridional overturning circulation through Southern Ocean upwelling. *Nat. Geosci.*, **5**, 171–180, https://doi.org/10.1038/ngeo1391.

McCoy, D. T., D. L. Hartmann, and D. P. Grosvenor, 2014: Observed Southern Ocean cloud properties and shortwave reflection. Part I: Calculation of SW flux from observed cloud properties. *J. Climate*, **27**, 8836–8857, https://doi.org/10.1175/JCLI-D-14-00287.1.

——, and Coauthors, 2019: Cloud feedbacks in extratropical cyclones: Insight from long-term satellite data and high-resolution global simulations. *Atmos. Chem. Phys.*, **19**, 1147–1172, https://doi.org/10.5194/acp-19-1147-2019.

McCoy, I. L., R. Wood, and J. K. Fletcher, 2017: Identifying meteorological controls on open and closed mesoscale cellular convection associated with marine cold air outbreaks. *J. Geophys. Res. Atmos.*, **122**, 11 678–11 702, https://doi.org/10.1002/2017JD027031.

Mieslinger, T., Á. Horváth, S. A. Buehler, and M. Sakradzija, 2019: The dependence of shallow cumulus macrophysical properties on large-scale meteorology as observed in ASTER imagery. *J. Geophys. Res. Atmos.*, **124**, 11 477–11 505, https://doi.org/10.1029/2019JD030768.

Myers, T. A., R. C. Scott, M. D. Zelinka, S. A. Klein, J. R. Norris, and P. M. Caldwell, 2021: Observational constraints on low cloud feedback reduce uncertainty of climate sensitivity. *Nat. Climate Change*, **11**, 501–507, https://doi.org/10.1038/s41558-021-01039-0.

Norris, J. R., 1998a: Low cloud type over the ocean from surface observations. Part I: Relationship to surface meteorology and the vertical distribution of temperature and moisture. *J. Climate*, **11**, 369–382, https://doi.org/10.1175/1520-0442(1998)011<0369:LCTOTO>2.0.CO;2.

——, 1998b: Low cloud type over the ocean from surface observations. Part II: Geographical and seasonal variations. *J. Climate*, **11**, 383–403, https://doi.org/10.1175/1520-0442(1998)011<0383:LCTOTO>2.0.CO;2.

Nuijens, L., and B. Stevens, 2012: The influence of wind speed on shallow marine cumulus convection. *J. Atmos. Sci.*, **69**, 168–184, https://doi.org/10.1175/JAS-D-11-02.1.

O'Gorman, P., 2010: Understanding the varied response of the extratropical storm tracks to climate change. *Proc. Natl. Acad. Sci. USA*, **107**, 19 176–19 180, https://doi.org/10.1073/pnas.1011547107.

Pincus, R., S. Platnick, S. A. Ackerman, R. S. Hemler, and R. J. P. Hofmann, 2012: Reconciling simulated and observed views of clouds: MODIS, ISCCP, and the limits of instrument simulators. *J. Climate*, **25**, 4699–4720, https://doi.org/10.1175/JCLI-D-11-00267.1.

Platnick, S., M. D. King, S. A. Ackerman, W. P. Menzel, B. A. Baum, J. C. Riédi, and R. A. Frey, 2003: The MODIS cloud products: Algorithms and examples from Terra. *IEEE Trans. Geosci. Remote Sens.*, **41**, 459–473, https://doi.org/10.1109/TGRS.2002.808301.

Rieck, M., L. Nuijens, and B. Stevens, 2012: Marine boundary layer cloud feedbacks in a constant relative humidity atmosphere. *J. Atmos. Sci.*, **69**, 2538–2550, https://doi.org/10.1175/JAS-D-11-0203.1.

Riehl, H., 1947: Diurnal variation of cloudiness over the subtropical Atlantic Ocean. *Bull. Amer. Meteor. Soc.*, **28**, 37–40, https://doi.org/10.1175/1520-0477-28.1.37.

Schulz, H., R. Eastman, and B. Stevens, 2021: Characterization and evolution of organized shallow convection in the downstream North Atlantic trades. *J. Geophys. Res. Atmos.*, **126**, e2021JD034575, https://doi.org/10.1029/2021JD034575.

Scott, R. C., T. A. Myers, J. R. Norris, M. D. Zelinka, S. A. Klein, M. Sun, and D. R. Doelling, 2020: Observed sensitivity of low-cloud radiative effects to meteorological perturbations over the global oceans. *J. Climate*, **33**, 7717–7734, https://doi.org/10.1175/JCLI-D-19-1028.1.

Stephens, G. L., D. O'Brien, P. J. Webster, P. Pilewski, S. Kato, and J. Li, 2015: The albedo of Earth. *Rev. Geophys.*, **53**, 141–163, https://doi.org/10.1002/2014RG000449.

——, M. Z. Hakuba, M. Hawcroft, J. M. Haywood, A. Behrangi, J. E. Kay, and P. J. Webster, 2016: The curious nature of the hemispheric symmetry of the Earth's water and energy balances. *Curr. Climate Change Rep.*, **2**, 135–147, https://doi.org/10.1007/s40641-016-0043-9.

Stevens, B., and J.-L. Brenguier, 2009: Cloud-controlling factors: Low clouds. *Clouds in the Perturbed Climate System: Their Relationship to Energy Balance, Atmospheric Dynamics, and Precipitation*, J. Heintzenberg and R. Charlson, Eds., MIT Press, 173–196.

——, and S. E. Schwartz, 2012: Observing and modeling Earth's energy flows. *Surv. Geophys.*, **33**, 779–816, https://doi.org/10.1007/s10712-012-9184-0.

Stubenrauch, C., and Coauthors, 2013: Assessment of global cloud datasets from satellites: Project and database initiated by the GEWEX radiation panel. *Bull. Amer. Meteor. Soc.*, **94**, 1031–1049, https://doi.org/10.1175/BAMS-D-12-00117.1.

Voigt, A., B. Stevens, J. Bader, and T. Mauristen, 2013: The observed hemispheric symmetry in reflected shortwave irradiance. *J. Climate*, **26**, 468–477, https://doi.org/10.1175/JCLI-D-12-00132.1.

——, ——, ——, and ——, 2014: Compensation of hemispheric albedo asymmetries by shifts of the ITCZ and tropical clouds. *J. Climate*, **27**, 1029–1045, https://doi.org/10.1175/JCLI-D-13-00205.1.

Vonder Haar, T. H., and V. E. Suomi, 1971: Measurements of the Earth's radiation budget from satellites during a five-year period. Part I: Extended time and space means. *J. Atmos. Sci.*, **28**, 305–314, https://doi.org/10.1175/1520-0469(1971)028<0305:MOTERB>2.0.CO;2.

Wall, C. J., D. L. Hartmann, and P. Ma, 2017a: Instantaneous linkages between clouds and large-scale meteorology over the Southern Ocean in observations and a climate model. *J. Climate*, **30**, 9455–9474, https://doi.org/10.1175/JCLI-D-17-0156.1.

——, T. Kohyama, and D. L. Hartmann, 2017b: Low-cloud, boundary layer, and sea ice interactions over the Southern Ocean during winter. *J. Climate*, **30**, 4857–4871, https://doi.org/10.1175/JCLI-D-16-0483.1.

Wood, R., and C. S. Bretherton, 2006: On the relationship between stratiform low cloud cover and lower-tropospheric stability. *J. Climate*, **19**, 6425–6432, https://doi.org/10.1175/JCLI3988.1.

Young, M. J., 1967: Variability in estimating total cloud cover from satellite pictures. *J. Appl.* Meteor. Climatol., **6**, 573–579, https://doi.org/10.1175/1520-0450(1967)006<0573:VIETCC>2.0.CO;2.

Zelinka, M. D., T. A. Myers, D. T. McCoy, S. Po-Chedley, P. M. Caldwell, P. Ceppi, S. A. Klein, and K. E. Taylor, 2020: Causes of higher climate sensitivity in CMIP6 models. *Geophys. Res. Lett.*, **47**, e2019GL085782, https://doi.org/10.1029/2019GL085782.